Relativistic convergent close-coupling method applied to electron scattering from mercury

Christopher J. Bostock,* Dmitry V. Fursa, and Igor Bray
ARC Centre for Antimatter-Matter Studies, Curtin University, GPO Box U1987, Perth, Western Australia 6845, Australia
(Received 24 June 2010; published 23 August 2010)

We report on the extension of the recently formulated relativistic convergent close-coupling (RCCC) method to accommodate two-electron and quasi-two-electron targets. We apply the theory to electron scattering from mercury and obtain differential and integrated cross sections for elastic and inelastic scattering. We compared with previous nonrelativistic convergent close-coupling (CCC) calculations and for a number of transitions obtained significantly better agreement with the experiment. The RCCC method is able to resolve structure in the integrated cross sections for the energy regime in the vicinity of the excitation thresholds for the $(6s6p)\,^3P_{0,1,2}$ states. These cross sections are associated with the formation of negative ion (Hg^-) resonances that could not be resolved with the nonrelativistic CCC method. The RCCC results are compared with the experiment and other relativistic theories.

DOI: 10.1103/PhysRevA.82.022713 PACS number(s): 34.80.Dp, 34.80.Bm

I. INTRODUCTION

The recently formulated relativistic convergent close-coupling (RCCC) method has been applied to electron scattering from quasi-one-electron atoms [1,2] and also highly charged hydrogen-like ions [3]. In the latter case it has been used to resolve discrepancies between theory and experiment for the polarization of x rays emitted by hydrogen-like ions during electron impact excitation. Here we report on the extension of the RCCC method to accommodate electron scattering from two-electron targets and quasi-two-electron targets. We apply the theory to electron scattering from Hg which serves as a testing ground [4] for relativistic theories due to its high atomic number $Z = 80$. Furthermore, electron-mercury scattering plays an important practical role in the physics of fluorescent and high-intensity discharge lamps [5–7]. The main source of light from these lamps is the 254 nm UV radiation emitted when the $(6s6p)\,^3P_1^o$ state decays to the $(6s^2)\,^1S_0$ ground state. This optical transition is a clear indication of a breakdown of the nonrelativistic approximation due to the strong spin-orbit interaction in Hg resulting in a significant singlet-triplet mixture for the Hg $6P_1^o$ states. In Hg fluorescent lamps this 254 nm radiation is absorbed by a phosphor coating which, in turn, emits visible light.

Accurate plasma physics modeling of Hg-based lamps requires detailed information on a large number of electron impact excitation cross sections involving transitions between various states. Compilation of e-Hg cross sections obtained from swarm data by [8] is widely used in plasma modeling to date even though more recent measurements for a number of transitions [9,10] are found to be in large disagreement with the former data. Given the difficulty in obtaining the comprehensive set of cross sections by experiment alone, a theoretical description of e-Hg scattering plays an important role in verifying the accuracy of the currently used cross sections and also establishing a new accurate set of e-Hg cross sections.

Previously we have applied the nonrelativistic convergent close-coupling (CCC) method to calculations of e-Hg scattering [11]. We have approximately taken into account the most important relativistic effects by transformation of the scattering amplitudes to an intermediate coupling scheme which allowed us to obtain cross sections for a wide range of transitions. While generally we obtained good agreement between the CCC results and the available experimental data there were a number of cases where the CCC results were either in disagreement with the experiment [e.g., elastic scattering differential cross section (DCS) at 15 eV] or could not be reliably applied to a calculation of particular transitions due to the inaccuracy of the approximate treatment of relativistic effects [e.g., excitation of$(6s6p)\,^3P_j^o$ fine-structure sublevels near the excitation threshold]. With development of the RCCC method we are now in a position to perform e-Hg calculations without any approximation in the treatment of relativistic effects both in the target structure and scattering calculations.

There is a long history of previous experimental and theoretical studies of electron scattering from Hg. Experimentally, integrated cross sections in the excitation threshold region of the triplet $(6s6p)\,^3P_{0,1,2}^o$ states have been measured in [12–17]. Integrated excitation cross sections for excitation of the singlet $(6s6p)\,^1P_1^o$ state have been measured in [9,10,18]. Integrated cross sections for excitation of $(6s7s)\,^1S_0$ and $(6s7p)\,^1P_1^o$ states have been measured in [9], and angle differential cross sections for elastic scattering from the $(6s^2)\,^1S_0$ ground state have been measured in [10,19]. Angle differential cross sections at 15 eV for excitation of the triplet $(6s6p)\,^3P_{0,1,2}^o$ states and singlet $(6s6p)\,^1P_1^o$ have been measured in [10]. At 60 eV, angle differential cross sections for the $(6s6p)\,^3P_1^o$ and $(6s6p)\,^1P_1^o$ states have been measured in [9,18]. The authors of [9] have also measured angle differential cross sections for the $(6s7s)\,^1S_0$ and $(6s7p)\,^1P_1^o$ states at this energy. Total cross section measurements have been obtained in [20], and elastic cross sections have been measured in [9,19,21]. Elastic momentum transfer cross sections have been measured in [9,22,23]. These play an important role in determining the electrical characteristics of discharge lamps. There are also extensive spin-dependent measurements for electron-mercury scattering [4].

On the theoretical side, in addition to the nonrelativistic CCC method employed in [11], there have been many other

*c.bostock@curtin.edu.au

attempts to model electron scattering from Hg. Some of these include the potential scattering models in [24–28]. The authors of [29] used the generalized Kohn-Sham method. Close-coupling calculations have also been performed: A five-state semirelativistic Breit-Pauli R-matrix method has been used in [30–32] to calculate excitation cross sections of the $6s6\,p\,^1P_1$ and $6s6\,p\,^3P_{0,1,2}$ states. The authors of [33] used a five-state relativistic Dirac R-matrix method to study resonances and also calculated elastic cross sections and excitation cross sections for the $(6s6p)\,^3P_{0,1,2}$ states. The excitation of the $6s6\,p^1P_1$ state has been studied in [34] using a semirelativistic distorted-wave Born approximation and also in [35] using a fully relativistic distorted-wave method.

Recently, the authors of [36] performed a 36-state Dirac B-spline R-matrix (DBSR) close-coupling calculation for electron scattering from Hg. They have reported a significant improvement in agreement with the experiment over previous calculations especially at low-threshold and near-threshold energies. Overall, the DBSR calculations are in good agreement with the nonrelativistic CCC results for incident electron energies above the threshold region. The important feature of the DBSR method is its ability to describe accurately the Hg target structure by allowing the opening of the $[\mathrm{Xe}]4f^{14}5d^{10}$ core. On other hand, in the CCC method (similar to practically all other calculations) the Hg atom was modeled as an atom with two active electrons above a frozen core $[\mathrm{Xe}]4f^{14}5d^{10}$. With the uncertainty of the approximate treatment of relativistic effects in the CCC method now removed in the RCCC method, we can now investigate whether the frozen-core model of Hg is sufficient to provide an accurate description of scattering near the thresholds of the $(6s6p)\,^3P_{0,1,2}$ triplet states. Similarly, the new RCCC calculations of e-Hg scattering will also be able to verify the accuracy of our previous nonrelativistic calculations for the transitions that are strongly affected by relativistic effects.

This paper is organized as follows. The next section contains the formulation of the RCCC method applicable to two-electron and quasi-two-electron targets, and the following section presents RCCC results for integrated and angle differential cross sections for elastic and inelastic electron collisions with Hg. Also presented are total, elastic, and momentum transfer cross sections. Atomic units are assumed throughout.

II. RCCC METHOD FOR TWO-ELECTRON TARGETS

Application of the RCCC method to electron scattering from Hg follows the same general scheme as described in [1,2]. Briefly, the target Hamiltonian is diagonalized in a Dirac L-spinor basis and then the obtained target states are used as an expansion basis to generate a set of coupled Lippmann-Schwinger equations for the electron-atom/ion scattering system. The latter are solved in momentum space for the T-matrix elements from which the cross sections are calculated.

For the case of electron scattering from Hg, the target atom is modeled as a quasi-two-electron atom consisting of two valence electrons above an inert $[\mathrm{Xe}]4f^{14}5d^{10}$ frozen core. The next two sections outline the calculation of the target states and then the theory required to set up and solve the coupled Lippmann-Schwinger equations for the scattering problem.

A. Target structure

The calculation of target wave functions and energy levels for two valence electrons above an inert $[\mathrm{Xe}]4f^{14}5d^{10}$ frozen core involves the three steps listed below.

1. The $[\mathrm{Xe}]4f^{14}5d^{10}$ frozen-core orbitals $\{\varphi_c\}$ are calculated with the GRASP package [37] that employs a relativistic self-consistent field Dirac-Fock procedure.
2. The Hg^+ one-electron Hamiltonian

$$H_i = c\,\boldsymbol{\alpha}\cdot\boldsymbol{p}_i + \beta mc^2 + V_i, \tag{1}$$

is then diagonalized with a Dirac L-spinor basis [38]

$$f^{\mathrm{L/S}}_{n_r\kappa}(r) = \left[\frac{n_r!(2\gamma+n_r)}{2N_{n_r\kappa}(N_{n_r\kappa}-\kappa)\Gamma(2\gamma+n_r)}\right]^{1/2}(2\lambda r)^{\gamma}e^{-\lambda r} \times\left[-(1-\delta_{n_r,0})L^{2\gamma}_{n_r-1}(2\lambda r)\pm\frac{N_{n_r\kappa}-\kappa}{n_r+2\gamma}L^{2\gamma}_{n_r}(2\lambda r)\right], \tag{2}$$

with the method outlined in detail in [2] for quasi-one-electron targets. Briefly, V_i is the interaction of one of the valence electrons with a closed core and is a sum of a frozen-core Dirac-Fock potential V^{FC} and a polarization potential V^{pol},

$$V_i = V^{\mathrm{FC}} + V^{\mathrm{pol}}. \tag{3}$$

The nonlocal V^{FC} potential is defined as a sum of local (direct) V^{FC}_d and nonlocal (exchange) terms

$$V_i = V^{\mathrm{FC}}_d + V^{\mathrm{FC}}_e, \tag{4}$$

with

$$V^{\mathrm{FC}}_d\phi(\boldsymbol{r}_i) = \left[-\frac{Z}{r}+\sum_{\varphi_c}\int d^3r'\frac{|\varphi_c(\boldsymbol{r}')|^2}{|\boldsymbol{r}-\boldsymbol{r}'|}\right]\phi(\boldsymbol{r}_i), \tag{5}$$

$$V^{\mathrm{FC}}_e\phi(\boldsymbol{r}_i) = -\sum_{\varphi_c}\int d^3r'\frac{\varphi_c(\boldsymbol{r}')^*\phi(\boldsymbol{r}'_i)}{|\boldsymbol{r}-\boldsymbol{r}'|}\varphi_c(\boldsymbol{r}'). \tag{6}$$

3. The set of electron orbitals $\{\phi_\alpha\}$ so obtained are used to perform standard configuration-interaction calculations [39] to obtain a set of Hg target states.

In this last step, the method employed to perform the configuration interaction calculation is similar to that described in detail in [39] with the exception that the jj coupling scheme is utilized in the relativistic formulation. Therefore the Hg target states are expressed as

$$\Phi_n(\boldsymbol{r}_1,\boldsymbol{r}_2) = \sum_{\alpha\beta}C^{(n)}_{\alpha\beta}\langle\boldsymbol{r}_1\boldsymbol{r}_2|\phi_\alpha(1)\phi_\beta(2):J_{T_n}m_n\pi_n\rangle, \tag{7}$$

where the configuration interaction coefficients $C^{(n)}_{\alpha\beta}$ satisfy

$$C^{(n)}_{\alpha\beta} = (-1)^{j_\alpha+j_\beta-J_n}C^{(n)}_{\beta\alpha}, \tag{8}$$

to ensure antisymmetry of the two-electron target states. The parity of the target states is $\pi = (-1)^{l_\alpha+l_\beta}$ and

$$|j_\alpha j_\beta : J_n m_n\rangle = \sum_{m_\alpha m_\beta}C^{J_n m_n}_{j_\alpha m_\alpha j_\beta m_\beta}|j_\alpha m_\alpha j_\beta m_\beta\rangle, \tag{9}$$

where $C^{J_n m_n}_{j_\alpha m_\alpha j_\beta m_\beta}$ is a Clebsch-Gordan coefficient. The target states $\Phi_n(\boldsymbol{r}_1,\boldsymbol{r}_2)$ satisfy

$$\langle\Phi_{n'}|H_T|\Phi_n\rangle = \epsilon_n\delta_{n'n}, \tag{10}$$

where

$$H_T = H_1 + H_2 + V_{12}, \tag{11}$$

with

$$V_{12} = 1/|\boldsymbol{r}_1 - \boldsymbol{r}_2| + V^{\rm diel}(\boldsymbol{r}_1,\boldsymbol{r}_2), \tag{12}$$

and the Dirac Hamiltonian for each electron H_i is given by Eq. (1). The phenomenological one-electron $V^{\rm pol}$ and two-electron $V^{\rm diel}$ core polarization potentials allows us to take into account more accurately the effect of closed inert shells on the active electron [11]. The cutoff radii $r_c^{\rm pol}$ and $r_c^{\rm diel}$ of these potentials are chosen to obtain the best representation of target-state energies and oscillator strength while the static dipole polarazability of the inert core α_c is taken either from the experiment or accurate calculations. In the case of Hg we chose $\alpha_c = 8.4$, $r_c^{\rm pol} = 2.235$, and $r_c^{\rm diel} = 2.3$.

Using a Dirac L-spinor basis Eq. (2), consisting of 35 functions for each value of $\kappa = l$ and $\kappa = -l-1$ for $l = 0,1,2,3$ with an exponential fall-off parameter of 3.5, we diagonalized the Hg^+ Hamiltonian for each value of κ and obtained a set of Hg^+ one-electron orbitals $\{\phi_\alpha\}$. These orbitals are then used to perform standard two-electron configuration interaction (CI) calculations. Similar to our previous nonrelativistic calculations we find that the Hg bound states are well described in a model where the inner electron is limited to the $6s$ and $6p$ orbitals of the Hg^+ ion. The energy levels obtained for the first 15 lowest-lying states are listed in Table I and found to be in good agreement with the experimental energies in the NIST database [40]. A further check of the target wave-function accuracy is provided by optical oscillator strengths. The experimental value for the $(6s6p)\,^1P_1^o$ oscillator strength is 1.16 and it is in good agreement with our result of 1.20, while for the $(6s6p)\,^3P_1^o$ state the experimental value of 0.024 is lower than our result of 0.038. The ground-state static-dipole polarizability of the Hg atom is dominated by the $(6s6p)\,^1P_1^o$ state and in our structure model has a value of $\alpha_d = 22.6$, which is similar to the value obtained in nonrelativistic CCC calculations [11] and is significantly lower than the experimental value of $\alpha_d = 34.4$ [41]. This difference arises from opening of the $5d^{10}$ shell, which is not allowed in the present model and can lead to inaccuracy in the calculated cross sections (see [11] for more discussion).

In the consequent scattering calculations we have used two models: the 29 state model (RCC) that includes only bound states in the close-coupling expansion and a 193 state model (RCCC) which in addition has a large number of positive energy states (relative to the Hg^+ ground state) which allows us to model coupling to ionization channels.

B. Coupled relativistic Lippmann-Schwinger equations

Once the target states are obtained the next step is to use them to generate a set of coupled relativistic Lippmann-Schwinger equations for the scattering problem. The total scattering wave function for the system satisfies

$$(E^{(+)} - H)|\Psi_i^{(+)}\rangle = 0, \tag{13}$$

where the superscript (+) denotes the incoming plane-wave or Coulomb-wave and outgoing spherical-wave boundary conditions. We denote the initial target state as Φ_i and the projectile momentum by k_i.

The total Hamiltonian for the scattering system is

$$H = H_T - H_0 - V_{01} - V_{02}, \tag{14}$$

where the subscript 0 denotes the projectile electron, 1 and 2 denote the electrons in the two-electron target, and H_T is given by Eq. (11).

The projectile Hamiltonian is given by

$$H_0 = c\,\boldsymbol{\alpha}\cdot\boldsymbol{p}_0 + \beta mc^2 + V_0. \tag{15}$$

To ensure antisymmetry of the total wave function in accordance with the Pauli exclusion principle, we perform a multichannel expansion of the total wave function in the following way:

$$\begin{aligned}\Psi_i^{N(+)}(\boldsymbol{r}_0,\boldsymbol{r}_1,\boldsymbol{r}_2) &= (1 - P_{01} - P_{02})\psi_i^{N(+)}(\boldsymbol{r}_0,\boldsymbol{r}_1,\boldsymbol{r}_2)\\ &= (1 - P_{01} - P_{02})\sum_{n=1}^{N} f_n^N(\boldsymbol{r}_0)\Phi_n^N(\boldsymbol{r}_1,\boldsymbol{r}_2),\end{aligned} \tag{16}$$

where P_{0i} is the space exchange operator. The RCCC method utilizes the completeness of the Dirac L-spinor basis used in the diagonalization of the target

$$\lim_{N\to\infty}\Psi^{N(+)}(\boldsymbol{r}_0,\boldsymbol{r}_1,\boldsymbol{r}_2) = \Psi^{(+)}(\boldsymbol{r}_0,\boldsymbol{r}_1,\boldsymbol{r}_2). \tag{17}$$

Substituting Eqs. (16) and (14) into Eq. (13) we obtain

$$\begin{aligned}&[E^{(+)} - c\,\boldsymbol{\alpha}\boldsymbol{p}_0 - \beta mc^2 - U_0 - H_T - U_0]\Psi^{N(+)}(\boldsymbol{r}_0,\boldsymbol{r}_1,\boldsymbol{r}_2)\\ &\quad = V\Psi^{N(+)}(\boldsymbol{r}_0,\boldsymbol{r}_1,\boldsymbol{r}_2),\end{aligned} \tag{18}$$

TABLE I. Energy levels of the first 15 Hg states calculated by diagonalizing the target in the RCCC method. Experiment levels listed by NIST [40] are also shown.

Configuration	Term	J	Parity	Energy (eV)	Expt. [40]
$6s^2$	$^1S_0$	0.0	1	0.000	0.000
$6s6p$	$^3P_0^o$	0.0	−1	4.706	4.667
$6s6p$	$^3P_1^o$	1.0	−1	4.926	4.887
$6s6p$	$^3P_2^o$	2.0	−1	5.577	5.461
$6s6p$	$^1P_1^o$	1.0	−1	6.549	6.704
$6s7s$	$^3S_1$	1.0	1	7.775	7.730
$6s7s$	$^1S_0$	0.0	1	8.000	7.926
$6s7p$	$^3P_0^o$	0.0	−1	8.648	8.619
$6s7p$	$^3P_1^o$	1.0	−1	8.667	8.637
$6s7p$	$^3P_2^o$	2.0	−1	8.763	8.829
$6s7p$	$^1P_1^o$	1.0	−1	8.872	8.839
$6s6d$	$^3D_1$	1.0	1	8.869	8.845
$6s6d$	$^1D_2$	2.0	1	8.876	8.844
$6s6d$	$^3D_3$	3.0	1	8.883	8.856
$6s6d$	$^3D_2$	2.0	1	8.887	8.852
Ionization limit				10.447	10.438

where

$$V = V_0 - U_0 + V_{01} + V_{02} + (E - H)(P_{01} + P_{02}). \quad (19)$$

The introduction of an arbitrary short-range (distorting) potential U_0 is used as a numerical technique to reduce the required computational resources, the results are independent of U_0. This rearrangement is such that the asymptotic (large r_0) Hamiltonian is

$$H_a = c\,\boldsymbol{\alpha}\cdot\boldsymbol{p}_0 + \beta mc^2 + U_0 + H_T. \quad (20)$$

The asymptotic Hamiltonian is used to generate the Green's function for the total wave function, as described in detail in [2], the Green's function is then used to generate a set of coupled relativistic Lippmann-Schwinger equations in momentum space for each total angular momentum J and parity Π of the system

$$T_{fi}^{\Pi J}(k_f\kappa_f, k_i\kappa_i) = V_{fi}^{\Pi J}(k_f\kappa_f, k_i\kappa_i) + \sum_n \sum_\kappa \int\!\!\!\!\!\!\diagup\!\!\!\!\!\!\int k^2 dk \times \frac{V_{fn}^{\Pi J}(k_f\kappa_f, k\kappa) T_{ni}^{\Pi J}(k\kappa, k_i\kappa_i)}{E - \epsilon_n^N - \epsilon_{k'} + i0}. \quad (21)$$

The relativistic V-matrix elements of the operator in Eq. (19) for a two-electron target are given explicitly in the Appendix.

The numerical calculation of the V-matrix elements and the solution of the coupled relativistic Lippmann-Schwinger equations is achieved with a parallelized computer code that employs a hybrid OpenMP-MPI scheme. Standard SCALAPACK routines [42] solve the set of linear equations (the coupled Lippmann-Schwinger equations) given by Eq. (21) for the T-matrix elements. Calculations were done with 20 partial waves and then the analytical Born subtraction technique [2] was used to account for higher partial waves. Observables such as cross sections can be calculated from the T-matrix elements using the equations specified in [2].

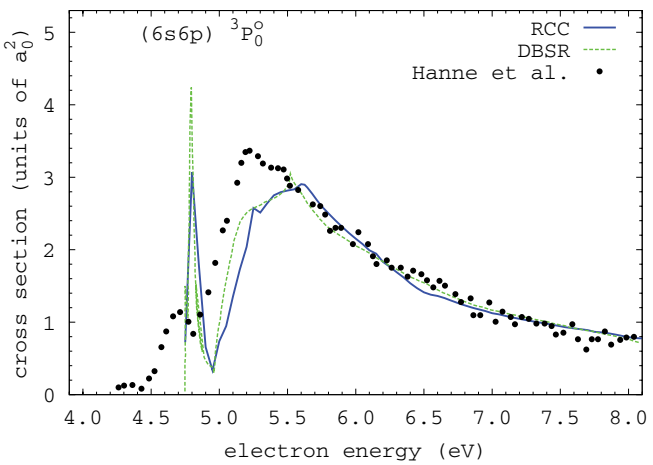

FIG. 1. (Color online) RCCC integrated excitation cross section for the $(6s6p)\,^3P_0^o$ state. Also shown are DBSR results [36] and the experimental results found in [12].

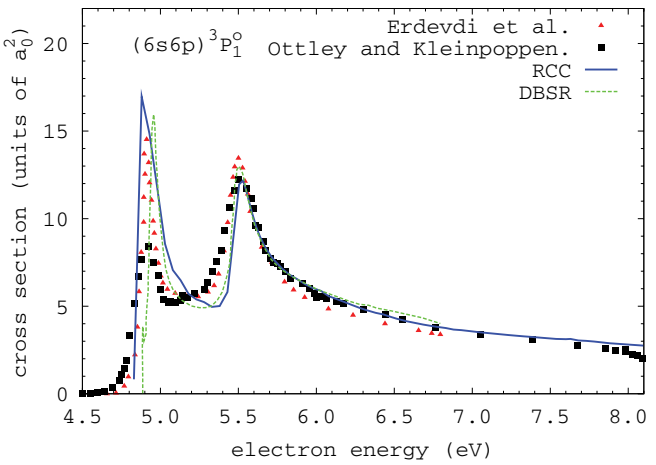

FIG. 2. (Color online) RCCC integrated excitation cross section for the $(6s6p)\,^3P_1^o$ state. Also shown are DBSR results [36] and experimental results found in [13,14].

III. RESULTS

A. Integrated cross sections for excited states

As discussed in the previous section, we have performed calculations in two models: RCC and RCCC. We found that for incident electron energies below 8 eV the inclusion of the continuum states made negligible difference to the calculated cross sections and will present only RCC results at these low energies.

We begin by presenting integrated cross sections for the $(6s6p)\,^3P_{0,1,2}^o$ states of Hg at low energies. Calculation of these cross sections at energies close to the excitation threshold was not possible with the nonrelativistic CCC method. Figure 1 shows the RCCC integrated cross section for the excitation of the $(6s6p)\,^3P_0^o$ triplet state. In the energy regime near the excitation threshold of these states the cross sections are dominated by the formation of negative ion (Hg^-) resonant states [43,44]. There is excellent agreement between the RCCC results and the DBSR calculations found in [36]. The RCCC results are also generally in good agreement

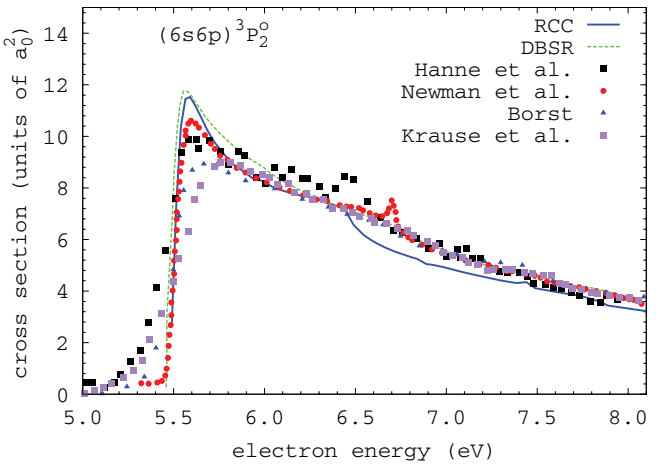

FIG. 3. (Color online) RCCC-integrated excitation cross section for the $(6s6p)\,^3P_2^o$ state. Also shown are DBSR results [36] and experimental results found in [12,15–17].

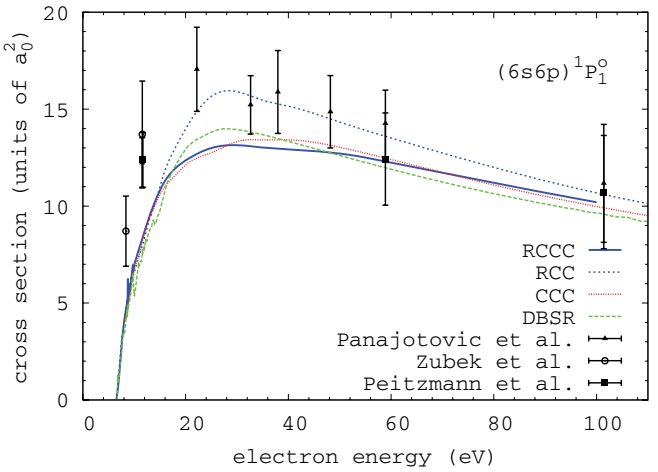

FIG. 4. (Color online) RCCC-integrated excitation cross section for the singlet $(6s6p)\,^1P_1^o$ state. Also shown are nonrelativistic CCC results [11], DBSR results [36], and experimental results found in [9,10,18].

with the measurements found in [12]. Note in Table I the RCCC energies for the triplet states are slightly different (<0.12 eV) from the experimental values and therefore the position of the resonances had to be offset in the figures by the same amount to align with the experimental position of the resonances.

Figure 2 shows the integrated cross section for excitation of the $(6s6p)\,^3P_1^o$ triplet state. The RCCC results are in very good agreement with both the DBSR calculations in [36] and the measurements in [13,14].

The integrated cross section for excitation of the $(6s6p)\,^3P_2^o$ triplet state is shown in Fig. 3. Once again very good agreement is found between the RCCC results and DBSR results [36] and also the measurements in [12,15–17], however, in the region between 6.5 and 7.5 eV the RCCC results are slightly lower than the DBSR results and experiment. We verified the convergence of our calculations at this energy region. The possible explanation for the discrepancy is likely to be related

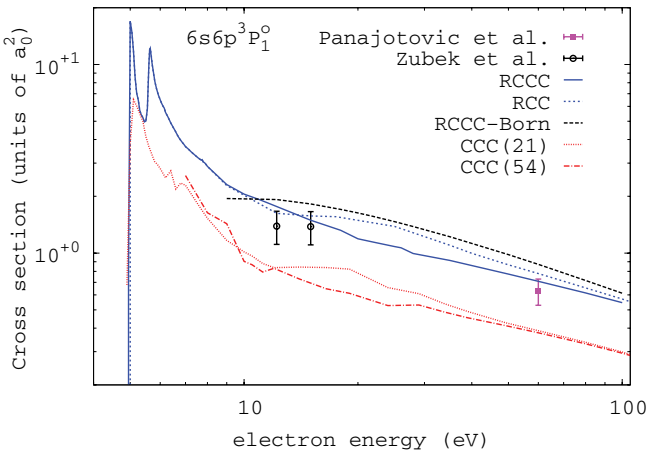

FIG. 5. (Color online) RCCC-integrated excitation cross section for the singlet $(6s6p)\,^3P_1^o$ state. Also shown are nonrelativistic CCC results [11] and experimental results found in [9,10,18].

to the error in the $^1P_1^o - {}^3P_2$ energy difference for our target model which leads to a loss of flux to the $^1P_1^o$ state which opens at 0.25 eV below the correct energy.

The integrated cross section for electron impact excitation of the singlet $(6s6p)\,^1P_1^o$ state is shown in Fig. 4. The difference between the RCC and RCCC calculations in this figure for intermediate and higher projectile energies gives an indication of the importance of coupling to the target continuum. The RCC calculation includes only the 29 discrete states and the cross section is higher by approximately 20% at the cross-section maximum than that obtained by the full RCCC calculation. In the vicinity of 8.6 eV, very small resonance structures are present in the $(6s6p)\,^1P_1^o$ cross section for both the RCCC and DBSR results.

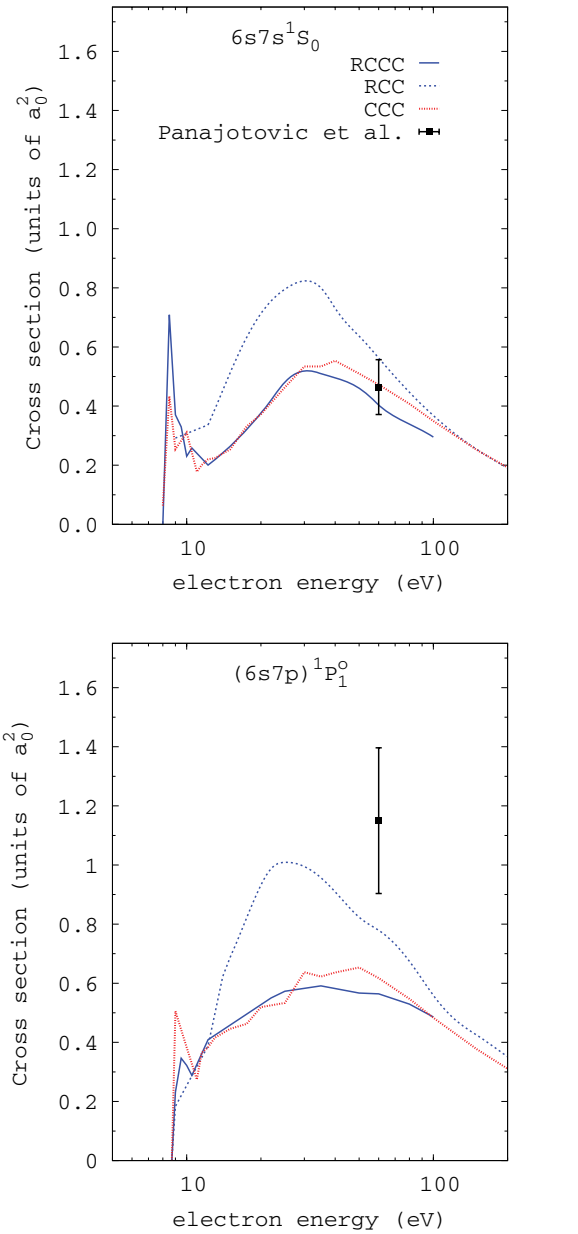

FIG. 6. (Color online) RCCC and nonrelativistic CCC [11] integrated cross sections for excitation of $(6s7s)\,^1S_0$ and $(6s7p)\,^1P_1^o$ states. Experiment is found in [9].

In Fig. 5 we present integrated cross sections for the $(6s6p)\,^3P_1^o$ state over a large energy range. We can see the substantial difference between the present RCCC results and nonrelativistic CCC results. This difference signifies the importance of an accurate account of relativistic effects for this transition. The present RCCC results are in good agreement with the experimental estimate of this cross section in [9,10]. Similar to the nonrelativistic results we find that coupling to ionization channels plays a relatively minor role as RCCC and RCC results are close (except in the 20–40 eV energy range). However, interchannel coupling plays a major role for this transition. The first-order approximation cross section, labeled RCCC-Born in Fig. 5, will be strongly dependent on the value for the optical oscillator strength. Given that the RCCC structure model for the $(6s6p)\,^3P_1^o$-$(6s^2)\,^1S^0$ transition has an optical oscillator strength value larger by about 50% than the experimental value we find that RCCC-Born result significantly overestimates the experiment. The good agreement between the RCCC results and experiment is a confirmation that high-order scattering effects are dominant for this transition.

Integrated cross sections for excitation of the $(6s7s)\,^1S_0$ and $(6s7p)\,^1P_1^o$ states are presented in Fig. 6. We find good agreement with our previous nonrelativistic CCC calculations. For these much smaller cross sections the coupling to the ionization continuum proved to be significantly more important as a comparison between the RCCC and RCC results clearly shows. A similar conclusion was drawn on the basis of nonrelativistic CCC calculations [11]. We can conclude that for these states relativistic effects play a minor role.

B. Angle differential cross sections for elastic and inelastic scattering

Angle differential cross sections for elastic scattering from the $(6s^2)\,^1S_0$ ground state of Hg are presented in Fig. 7. While

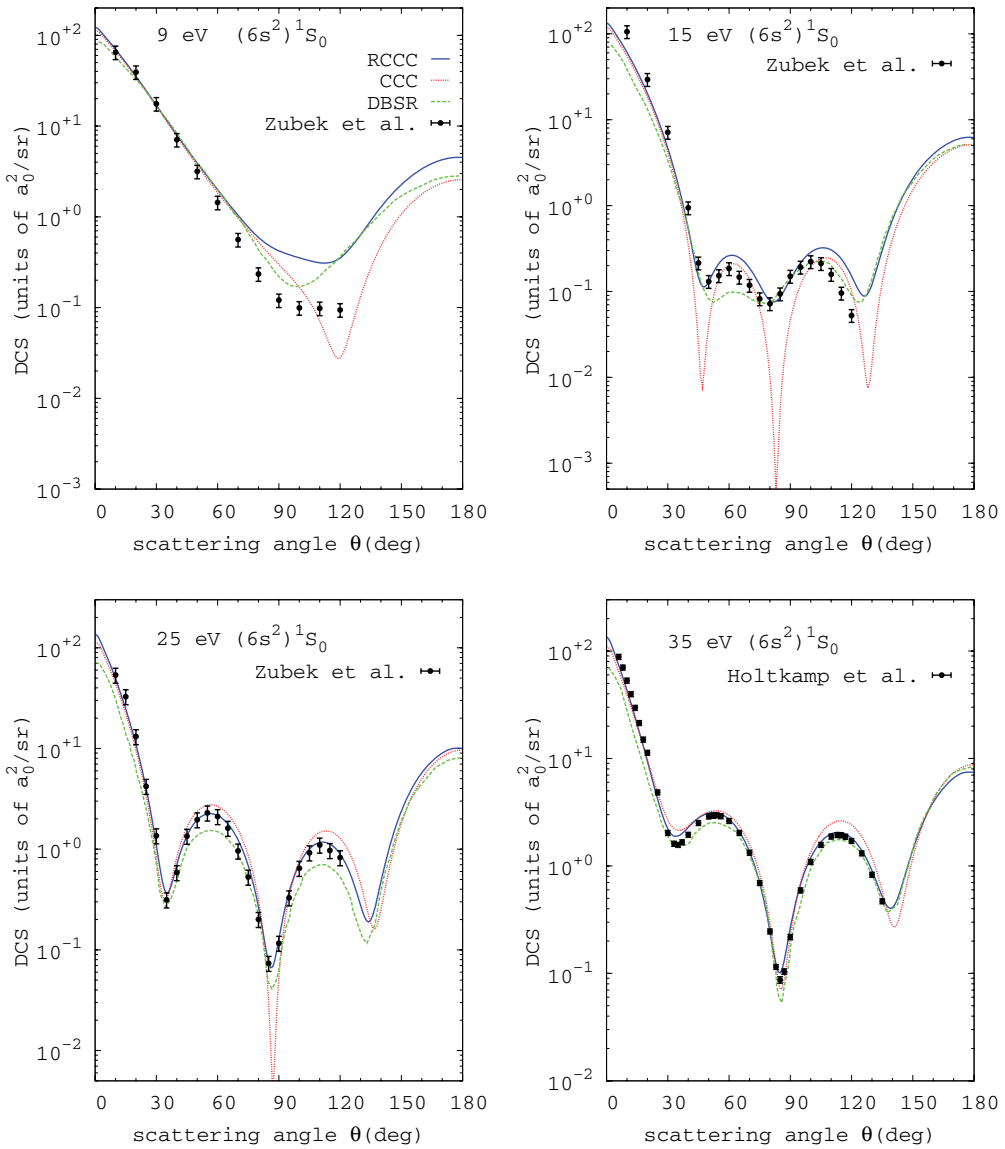

FIG. 7. (Color online) RCCC angle differential cross sections for elastic scattering from the $(6s^2)\,^1S_0$ ground state. Also shown are nonrelativistic CCC results [11], DBSR results [36], and experimental results found in [10,19].

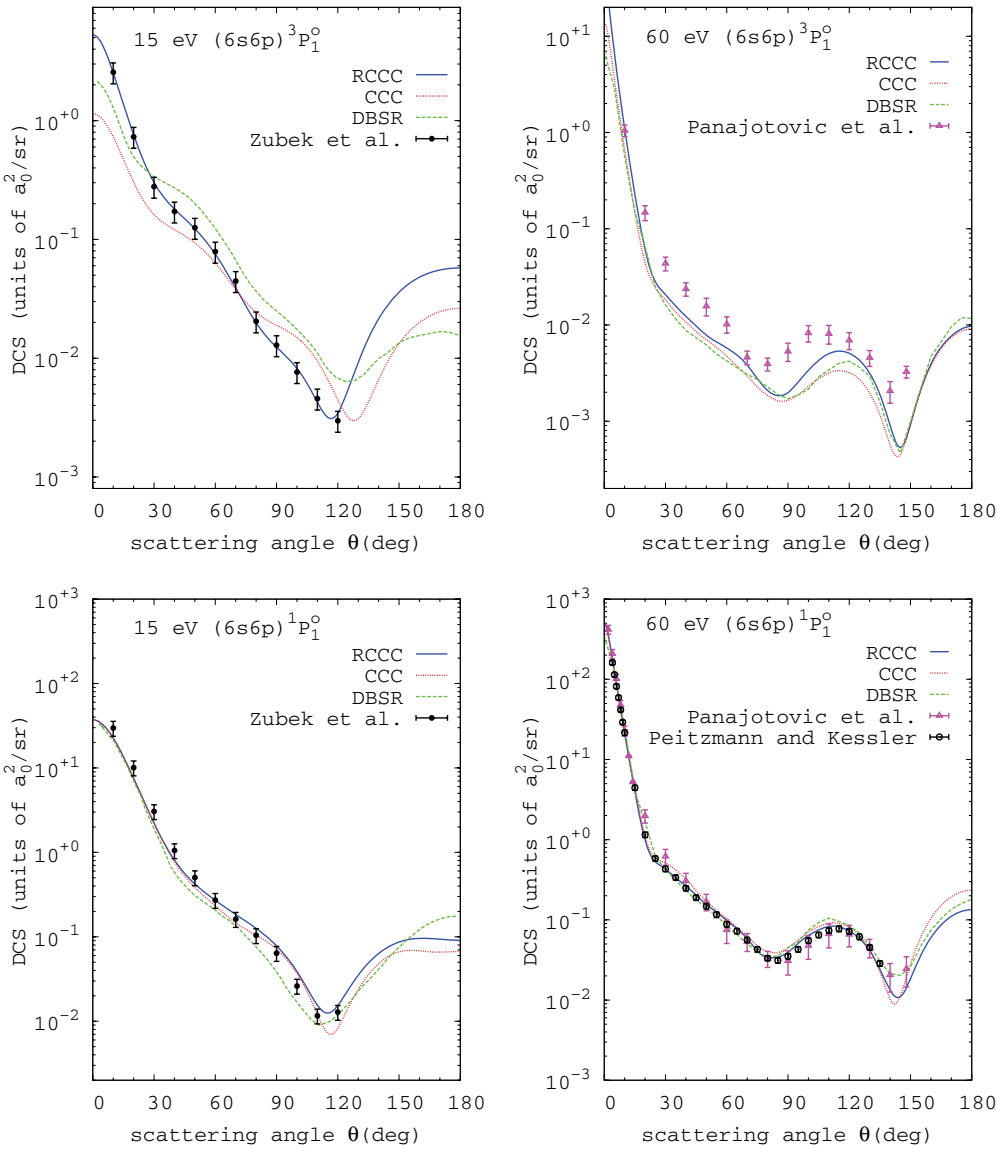

FIG. 8. (Color online) RCCC angle differential cross sections at 15 and 60 eV for the $(6s6p)\,^3P_1^o$ states and $(6s6p)\,^1P_1^o$ state. Also shown are nonrelativistic CCC results [11], DBSR results [36], and the experiment found in [9,10,18].

our previous nonrelativistic CCC calculations had difficulty in describing elastic cross section at 15 eV (the minima were too deep) the RCCC differential cross section do not have such a problem and are in very good agreement with the experiment [10] and also DBSR calculations [36]. As the incident electron energy increases to 25 and 35 eV we observe nearly perfect agreement between the theoretical and experimental results [19]. At 9 eV we observe good agreement between all theoretical results and experiment at forward scattering. However, the region around the cross-section minimum (100°–120°) proved to be particularly sensitive to the details of theoretical models with none of the available theories being in agreement with experiment.

In Fig. 8 we present angle differential cross sections at 15 and 60 eV for the$(6s6p)\,^3P_1^o$ and $(6s6p)\,^1P_1^o$ states. Excellent agreement is obtained with the measurements found in [10] for the $(6s6p)\,^1P_1^o$ and $(6s6p)\,^3P_1^o$ states at 15 eV. It is well known that the cross section for the $(6s6p)\,^1P_1^o$ state is strongly dependent on the accuracy of the optical oscillator strength for this transition [11] with channel coupling effects playing a rather minor role. For the $(6s6p)\,^3P_1^o$ state the situation apparently is quite different. The optical oscillator strength values in RCCC and DBSR calculations differ by a factor of two (0.038 and 0.018, respectively), however, a similar difference in differential cross sections can be observed only at forward scattering angles. Due to a small value of optical oscillator strength for this intercombinational transition an adequate account of the interchannel coupling becomes more important. Additionally, the difference between nonrelativistic and present relativistic RCCC results for this transition is an indication of the importance of an accurate treatment of relativistic effects in the calculation of target wave functions and the scattering process. As the incident electron energy increases to 60 eV we observe perfect agreement between all theoretical models (RCCC, CCC, DBSR) and the experiment for the $(6s6p)\,^1P_1^o$ state. For the $(6s6p)\,^3P_1^o$ state theoretical

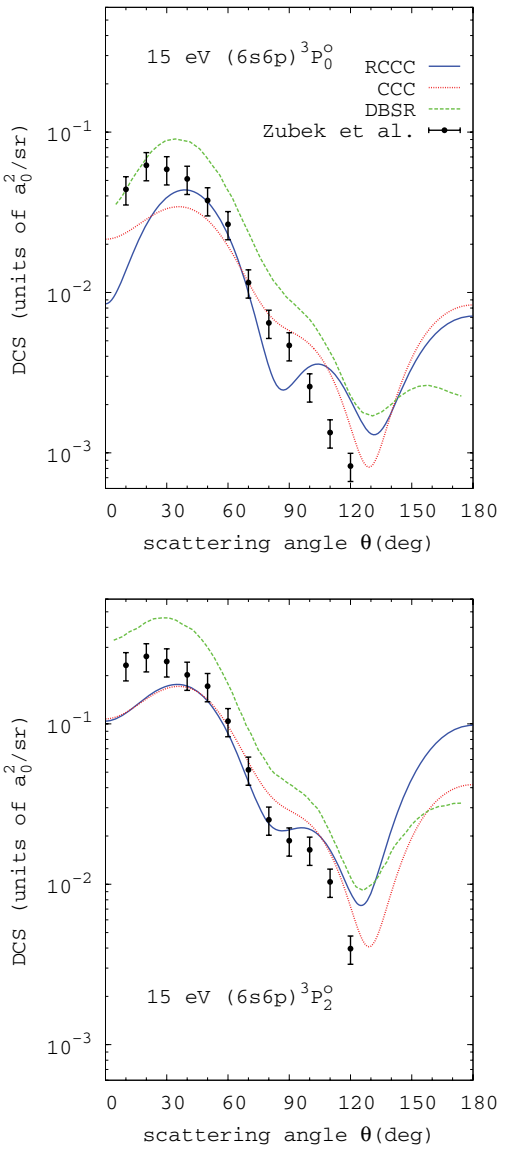

FIG. 9. (Color online) RCCC angle differential cross sections at 15 eV for the $(6s6p)\,^3P^o_0$ and $(6s6p)\,^3P^o_2$ states. Also shown are nonrelativistic CCC results [11], DBSR results [36], and experimental results found in [10].

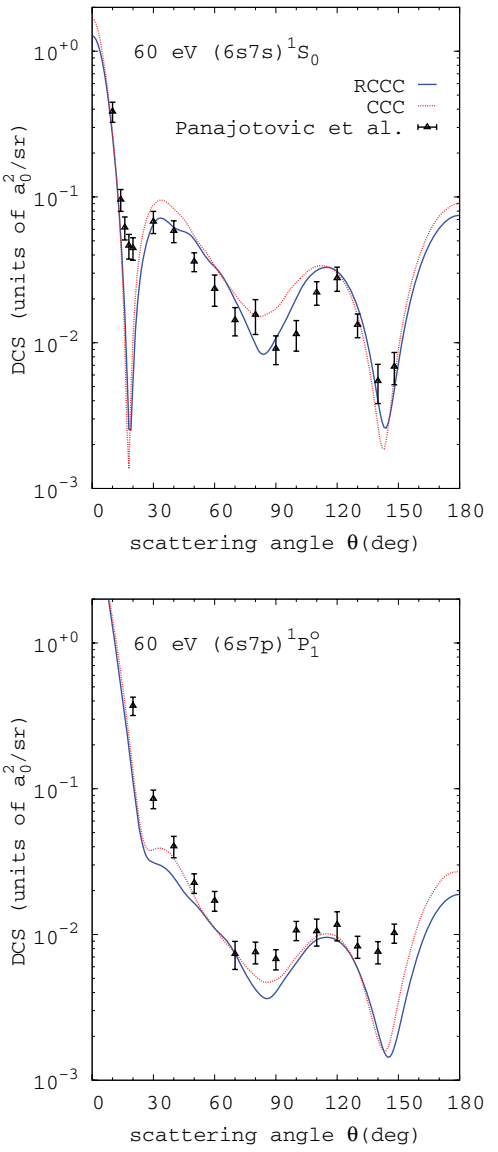

FIG. 10. (Color online) RCCC angle differential cross sections at 60 eV for the $(6s7s)\,^1S_0$ and $(6s7p)\,^1P^o_1$ states. Also shown are nonrelativistic CCC results [11] and the experiment found in [9].

results are in good agreement except for small scattering angles while the experimental results in [9] seem to be systematically higher. This situation is interesting as it contradicts the usual assumption that at this relatively large energy the singlet component of the target wave function would be dominant and therefore the $(6s6p)\,^1P^o_1$ and $(6s6p)\,^3P^o_1$ state cross sections are related simply by a multiplicative constant. It is worthwhile to note that this constant is not just a ratio of optical oscillator strength [1.16 and 0.024 are the experimental values for the $(6s6p)\,^1P^o_1$ and $(6s6p)\,^3P^o_1$ states, respectively] as the difference in excitation thresholds should be also taken into account which produces a cross section ratio coefficient of 18.7 (strictly valid for forward scattering only). However, rescaled in this way the $(6s6p)\,^1P^o_1$ cross section in [9] would be lower than their measured $(6s6p)\,^3P^o_1$ state cross section except for forward scattering angles. We note also that as the RCCC value for the $(6s6p)\,^3P^o_1$ state optical oscillator strength (0.038) is larger than the experimental value (0.024) and the DBSR value (0.018) is smaller than the experimental value one would expect that RCCC differential cross section for the $(6s6p)\,^3P^o_1$ state would overestimate the experiment while the DBSR results would underestimate it. In fact, this behavior is observed only at small scattering angles. This suggests that channel-coupling effects are still important at intermediate and large scattering angles at 60 eV and that they are captured adequately by the presented theoretical methods. On the other hand, the measurements of the $(6s6p)\,^3P^o_1$ state differential cross section [9] seem to be too high and a fresh look at the normalization procedure used appears to be warranted.

In Fig. 9 we present differential cross sections for the $(6s6p)\,^3P^o_0$ and $(6s6p)\,^3P^o_2$ states at 15 eV. We can see that nonrelativistic and relativistic CCC results are in reasonably good agreement, which supports the conclusion made in [11]

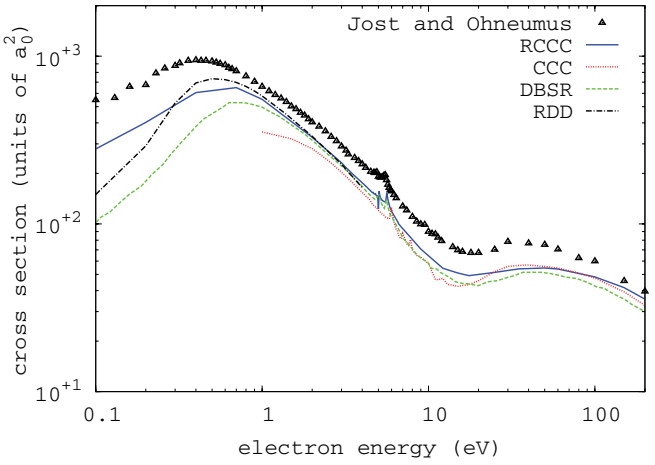

FIG. 11. (Color online) RCCC total cross section for scattering from the $(6s^2)\,{}^1S_0$ ground state of Hg. Also shown are nonrelativistic CCC results [11], DBSR results [36], and the experiment found in [20].

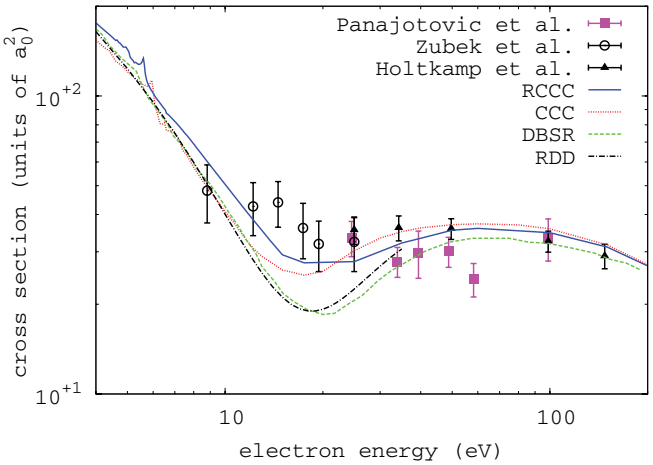

FIG. 12. (Color online) RCCC elastic cross section for scattering from the $(6s^2)\,{}^1S_0$ ground state of Hg. Also shown are nonrelativistic CCC results [11], DBSR results [36], and the experimental results found in [9,19,21].

that this transition is governed mostly by the exchange scattering. Our results are in good agreement with the measurements found in [10]. The results of DBSR calculations are somewhat larger than our results and the experiment which as discussed in [36] is most likely related to the lack of coupling to ionization channels in the DBSR model.

RCCC angle differential cross sections for the $(6s7s)\,{}^1S_0$ and $(6s7p)\,{}^1P_1^o$ states at 60 eV are shown in Fig. 10. The differential cross section for the $(6s7s)\,{}^1S_0$ state measured in [9] displays three minima which both the RCCC and CCC calculations predict in very good agreement with the experiment [9]. Interestingly, both the RCCC and CCC differential cross sections predict a very sharp first minimum. In contrast to the elastic scattering cross section (e.g., 15 eV) this appears to be a genuine feature which might be difficult to obtain experimentally due to the finite angular resolution. The RCCC and CCC results are also in excellent agreement for the differential cross section of the $(6s7p)\,{}^1P_1^o$ state and also in excellent agreement with the experiment [9] except for the angles near 150° at the second minimum in the cross section where the RCCC results are lower than the experimental values in the region of the minimum.

C. Total, elastic, and momentum transfer cross sections

In Fig. 11 we present the total cross section for electron scattering from the $(6s^2)\,{}^1S_0$ ground state of Hg, that is, the summed contribution from elastic, excitation, and ionization channels. We find that at energies above 2 eV the RCCC, CCC, and DBSR calculations are in excellent agreement with each other. We have also presented in this figure (below 4 eV) results of the calculations in [28] who used the polarized orbitals method with addition of a dynamic distortion potential [labeled RDD (relativistic dynamic distortion)]. At low energies all theoretical results have qualitatively similar behavior (maximum at about 0.4–0.5 eV) but show large variations in the cross section shape and absolute values. The difficulties in a theoretical description of low-energy e-Hg scattering have been recently highlighted in [36] and the present theoretical results should be considered with a degree of caution. The experiment in [20] shows good qualitative agreement with the RCCC results in terms of the shape of the cross section and the location of minima and maxima, however, the experimental cross section is consistently larger across all energies.

In Fig. 12 we present the elastic cross section. We find good agreement between the RCCC and CCC results and very good agreement with the experimental estimates of elastic cross sections in [9,19,21]. Comparing to other calculations we note that the cross section minimum at 20 eV in RCCC calculations is much shallower than in DBSR and RDD models and in better agreement with the experiment.

The RCCC elastic momentum transfer cross section for electron scattering on the ground state of Hg is presented in Fig. 13. At low energies, similar to the elastic integrated cross section, there is a wide variation in the results of the theoretical methods. The results of the RDD method are in

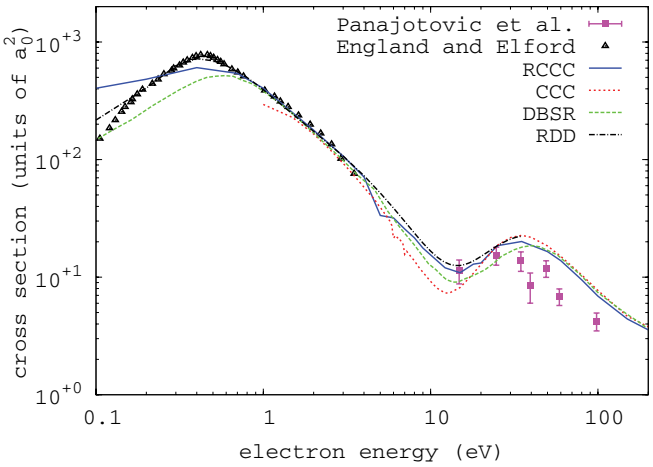

FIG. 13. (Color online) RCCC elastic momentum transfer section for scattering from the $(6s^2)\,{}^1S_0$ ground state of Hg. Also shown are the results of nonrelativistic CCC [11], DBSR [36] and RDD [28] calculations, and the experimental results found in [9,23].

excellent agreement with the experiment in [23] for the momentum transfer cross section, but interestingly, not for the integrated cross section. This suggests a possible inconsistency between the measurements in [20,23]. At energies above 1 eV RCCC, CCC, DBSR, and RDD results are in good agreement. Comparing with the experimental estimates in [9] we find that apart from the two lowest experimental points (at 15 and 25 eV) the experiment is systematically lower than the theoretical results.

IV. CONCLUSION

We have presented the steps required to formulate the RCCC method for quasi-two-electron targets and applied the theory to electron scattering from Hg, which is modeled as an atom with two active valence electrons above an inert ion core. In comparison with our previous study of e-Hg scattering using the nonrelativistic CCC method [11] confirmed the accuracy of the presented results for most of the considered transitions. In a number of cases where there was a discrepancy between CCC and the experimental results [e.g., elastic DCS at 15 eV and integrated cross section (ICS) for $(6s6sp)^3P_1^o$ state] we find that the fully relativistic approach is in much better agreement with the experiment. For scattering at energies close to the $(6s6p)\,^3P^o_{0,1,2}$ state thresholds, where nonrelativistic methods like CCC cannot be applied, we find very good agreement with the DBSR calculations and experiment.

Having demonstrated the accuracy of the RCCC method for e-Hg scattering we are now in a position to provide reliable scattering information of interest to various applications for quasi-two-electron targets. In the future we are also planning to apply the RCCC method to calculation of electron-photon correlations parameters and various spin asymmetries.

ACKNOWLEDGMENTS

The authors would like to thank K. Bartschat for useful discussions and O. Zatsarinny for sending DBSR data in electronic form. Resources of the Australian National Computational Infrastructure (NCI) Facility and its Western Australian node iVEC are gratefully acknowledged.

APPENDIX: RELATIVISTIC DIRECT AND EXCHANGE MATRIX ELEMENTS

The direct and exchange matrix elements for electron scattering from a two-electron target in the RCCC method differ from their nonrelativistic counterparts due to the fact that the LS coupling scheme is employed in the nonrelativistic case [39], whereas spin and orbital angular momenta are not decoupled in the relativistic case. Therefore we present here the explicit forms of the direct and exchange matrix elements used in the solution of the set of relativistic Lippmann-Schwinger equations, Eq. (21).

In a manner similar to the nonrelativistic case for two-electron targets [39,45] we may separate the V operator in Eq. (19) as

$$V = (V_0 - U_0 + 2V_{01}) + 2(E - H_T - H_0 - V_{01} - V_{02})P_{01}. \tag{A1}$$

The first term is the direct matrix element and the second term is the exchange matrix element.

We use the CI representation of the two-electron target wave functions to express the matrix elements

$$\begin{aligned}\langle j_0'k_0'(0),\Phi_{n'} : J'M_{J'}|V|j_0k_0(0),\Phi_n : JM_J\rangle \\ = \sum_{\alpha,\beta,\gamma,\delta} C^{(n')}_{\alpha\beta}C^{(n)}_{\gamma\delta}\langle j_0'k_0'(0),\phi_\alpha(1)\phi_\beta(2)(J_T') : J'M_{J'}| \\ \times V|j_0k_0(0),\phi_\gamma(1)\phi_\delta(2)(J_T) : JM_J\rangle.\end{aligned} \tag{A2}$$

A. Direct matrix elements

The direct matrix element is associated with the first term in Eq. (A1), which has the multipole expansion

$$\begin{aligned}V^D &= V_0 - U_0 + 2V_{01} \\ &= \sum_\nu v_\nu(r_0,r_1)\boldsymbol{C}^\nu(0)\cdot\boldsymbol{C}^\nu(1).\end{aligned} \tag{A3}$$

where

$$v_\nu(r_0,r_1) = -\delta_0^\nu\left[\frac{Z}{r_0} + U_0(r_0)\right] + 2\frac{r_<^\nu}{r_>^{\nu+1}}, \tag{A4}$$

and $\boldsymbol{C}^\nu$ is a renormalized spherical harmonic.

Using standard tensor algebra relations [46] the direct matrix element for each configuration pair reduces to

$$\begin{aligned}&\langle j_0'k_0'(0),\phi_\alpha(1)\phi_\beta(2)(J_T') : J'M_{J'}|\sum_\nu v_\nu\boldsymbol{C}^\nu(0)\cdot\boldsymbol{C}^\nu(1)|j_0k_0(0),\phi_\gamma(1)\phi_\delta(2)(J_T) : JM_J\rangle \\ &= \frac{1}{\pi}\sqrt{\frac{(\epsilon_{k'}+c^2)(\epsilon_k+c^2)}{\epsilon_{k'}\epsilon_k}}\langle\phi_\beta|\phi_\delta\rangle\delta_{JJ'}\delta_{M_JM_{J'}}\begin{Bmatrix} j_0' & J_T' & J' \\ J_T & j_0 & \nu\end{Bmatrix}\langle j_0'||\boldsymbol{C}^\nu(0)||j_0\rangle \\ &\times \hat{J}_T'\hat{J}_T\delta_{j_\beta j_\delta}(-1)^{j_\alpha+j_\beta+J_T+\nu+J_T'+j_0+J'}\begin{Bmatrix} j_\beta & j_\alpha & J_T' \\ \nu & J_T & j_\gamma\end{Bmatrix}\langle J_\alpha||\boldsymbol{C}^\nu(1)||J_\gamma\rangle \\ &\times \int dr_0\int dr_1\left\{\sum_\nu v_\nu(r_0,r_1)\left[f^U_{\kappa_0'}(r_0)f^U_{\kappa_0}(r_0) + f^L_{-\kappa_0'}(r_0)f^L_{-\kappa_0}(r_0)\right]\left[\phi^U_{\kappa_\alpha}(r_1)\phi^U_{\kappa_\gamma}(r_1) + \phi^L_{-\kappa_\alpha}(r_1)\phi^L_{-\kappa_\gamma}(r_1)\right]\right\},\end{aligned} \tag{A5}$$

where U and L denote the upper and lower components of the Dirac spinors and where

$$\langle\phi_\beta|\phi_\delta\rangle = \int dr_2\big[\phi^U_{\kappa_\beta}(r_2)\phi^U_{\kappa_\delta}(r_2) + \phi^L_{-\kappa_\beta}(r_2)\phi^L_{-\kappa_\delta}(r_2)\big], \quad \text{(A6)}$$

with

$$\hat{J} = \sqrt{2J+1}. \quad \text{(A7)}$$

B. Exchange matrix elements

The exchange matrix element is associated with the second term in Eq. (A1)

$$V_E = 2(E - H_T - H_0 - V_{01} - V_{02})P_{01}. \quad \text{(A8)}$$

We separate the calculation of the exchange matrix element into a number of steps.

1. $V_{01}P_{01}$ matrix elements

The first exchange matrix element for each configuration pair is

$$\langle j'_0k'_0(0),\phi_\alpha(1)\phi_\beta(2)(J'_T) : J'M_{J'}|V_{01}P_{01}|j_0k_0(0), \phi_\gamma(1)\phi_\delta(2)(J_T) : JM_J\rangle, \quad \text{(A9)}$$

where

$$V_{01} = \sum_\nu \frac{r^\nu_<}{r^{\nu+1}_>}\boldsymbol{C}^\nu(0)\cdot\boldsymbol{C}^\nu(1), \quad \text{(A10)}$$

We apply the space exchange operator P_{01} to the right-hand side and then recouple the angular momenta on the right-hand side using

$$|j_0,j_\gamma j_\delta(J_T) : J\rangle = \sum_j \hat{j}\hat{J}_T(-1)^{j_0+J_T+J_\gamma+j} \times \begin{Bmatrix} j_0 & j_\delta & j \\ j_\gamma & J & J_T \end{Bmatrix} |j_\gamma,j_0j_\delta(j) : J\rangle, \quad \text{(A11)}$$

to obtain

$$\begin{aligned}
&\langle j'_0k'_0(0),\phi_\alpha(1)\phi_\beta(2)(J'_T) : J'M_{J'}|V_{01}|j_0k_0(1),\phi_\gamma(0)\phi_\delta(2)(J_T) : JM_J\rangle \\
&= \frac{1}{\pi}\sqrt{\frac{(\epsilon_{k'}+c^2)(\epsilon_k+c^2)}{\epsilon_{k'}\epsilon_k}}\langle\phi_\beta|\phi_\delta\rangle\delta_{JJ'}\delta_{M_JM_{J'}}\delta_{j_\beta j_\delta}\hat{j}\hat{J}_T\hat{j}\hat{J}'_T(-1)^{j_0+J_T+2j_\gamma+2j+J'_T+J'+j_\alpha+j_\beta+\nu} \\
&\times \begin{Bmatrix} j_0 & j_\delta & j \\ j_\gamma & J & J_T \end{Bmatrix}\begin{Bmatrix} j'_0 & J'_T & J' \\ j & j_\gamma & \nu \end{Bmatrix}\begin{Bmatrix} j_\beta & j_\alpha & J'_T \\ \nu & j & j_0 \end{Bmatrix}\langle j'_0||\boldsymbol{C}^\nu(0)||J_\gamma\rangle\langle J_\alpha||\boldsymbol{C}^\nu(1)||j_0\rangle \\
&\times \int dr_0\int dr_1\left\{\sum_{\nu j}\frac{r^\nu_<}{r^{\nu+1}_>}\big[f^U_{\kappa'_0}(r_0)\phi^U_{\kappa_\gamma}(r_0) + f^L_{-\kappa'_0}(r_0)\phi^L_{-\kappa_\gamma}(r_0)\big]\big[\phi^U_{\kappa_\alpha}(r_1)f^U_{\kappa_0}(r_1) + \phi^L_{-\kappa_\alpha}(r_1)f^L_{-\kappa_0}(r_1)\big]\right\}. \quad \text{(A12)}
\end{aligned}$$

2. $V_{02}P_{01}$ matrix elements

The second exchange matrix element for each configuration pair is

$$\langle j'_0k'_0(0),\phi_\alpha(1)\phi_\beta(2)(J'_T) : J'M_{J'}|V_{02}P_{01}|j_0k_0(0), \phi_\gamma(1)\phi_\delta(2)(J_T) : JM_J\rangle, \quad \text{(A13)}$$

where

$$V_{02} = \sum_\nu \frac{r^\nu_<}{r^{\nu+1}_>}\boldsymbol{C}^\nu(0)\cdot\boldsymbol{C}^\nu(2). \quad \text{(A14)}$$

We apply P_{01} to the right-hand side, but this time it is convenient to recouple the angular momenta on the left-hand side to obtain

$$\begin{aligned}
&\langle j'_0k'_0(0),\phi_\alpha(1)\phi_\beta(2)(J'_T) : J'M_{J'}|V_{02}|j_0k_0(1),\phi_\gamma(0)\phi_\delta(2)(J_T) : JM_J\rangle \\
&= \frac{1}{\pi}\sqrt{\frac{(\epsilon_{k'}+c^2)(\epsilon_k+c^2)}{\epsilon_{k'}\epsilon_k}}\langle\phi_\alpha|j_0k_0\rangle\hat{J}_T\hat{J}'_T(-1)^{j'_0+J'_T+j_\alpha+j_\beta+j_\gamma}\begin{Bmatrix} j'_0 & j_\beta & J_T \\ j_\alpha & J' & J'_T \end{Bmatrix}\begin{Bmatrix} j'_0 & j_\beta & J_T \\ j_\delta & j_\gamma & \nu \end{Bmatrix}\langle j'_0||\boldsymbol{C}^\nu(0)||j_\gamma\rangle\langle j_\beta||\boldsymbol{C}^\nu(2)||j_\delta\rangle \\
&\times \int dr_0\int dr_2\left\{\sum_\nu\frac{r^\nu_<}{r^{\nu+1}_>}\big[f^U_{\kappa'_0}(r_0)\phi^U_{\kappa_\gamma}(r_0) + f^L_{-\kappa'_0}(r_0)\phi^L_{-\kappa_\gamma}(r_0)\big]\big[\phi^U_{\kappa_\beta}(r_2)\phi^U_{\kappa_\delta}(r_2) + \phi^L_{-\kappa_\beta}(r_2)\phi^L_{-\kappa_\delta}(r_2)\big]\right\}. \quad \text{(A15)}
\end{aligned}$$

3. $V_{12}P_{01}$ matrix elements

The third exchange matrix element for each configuration pair is

$$\langle j_0'k_0'(0),\phi_\alpha(1)\phi_\beta(2)(J_T') : J'M_{J'}|V_{12}P_{01}|j_0k_0(0),\phi_\gamma(1)\phi_\delta(2)(J_T) : JM_J\rangle, \tag{A16}$$

where

$$V_{12} = \sum_\nu \frac{r_<^\nu}{r_>^{\nu+1}} \boldsymbol{C}^\nu(1)\cdot\boldsymbol{C}^\nu(2). \tag{A17}$$

We apply P_{01} to the right-hand side and recouple the angular momenta on the right-hand side to obtain

$$\begin{aligned}&\langle j_0'k_0'(0),\phi_\alpha(1)\phi_\beta(2)(J_T') : J'M_{J'}|V_{12}|j_0k_0(1),\phi_\gamma(0)\phi_\delta(2)(J_T) : JM_J\rangle \\ &= \frac{1}{\pi}\sqrt{\frac{(\epsilon_{k'}+c^2)(\epsilon_k+c^2)}{\epsilon_{k'}\epsilon_k}}\langle j_0'k'|\phi_\gamma\rangle \hat{J}_T'\hat{J}_T(-1)^{2j_0+J_T+j_\gamma+j_\beta}\begin{Bmatrix} j_0 & j_\delta & J_T' \\ j_\gamma & J & J_T\end{Bmatrix}\begin{Bmatrix} j_\alpha & j_\beta & J_T' \\ j_\delta & j_0 & \nu\end{Bmatrix}\langle j_\alpha||\boldsymbol{C}^\nu(1)||j_0\rangle\langle j_\beta||\boldsymbol{C}^\nu(2)||j_\delta\rangle \\ &\times\int dr_1\int dr_2\left\{\sum_\nu \frac{r_<^\nu}{r_>^{\nu+1}}\left[\phi^U_{\kappa_\alpha}(r_1)f^U_{\kappa_0}(r_1)+\phi^L_{-\kappa_\alpha}(r_1)f^L_{-\kappa_0}(r_1)\right]\left[\phi^U_{\kappa_\beta}(r_2)\phi^U_{\kappa_\delta}(r_2)+\phi^L_{-\kappa_\beta}(r_2)\phi^L_{-\kappa_\delta}(r_2)\right]\right\}.\end{aligned} \tag{A18}$$

4. $(E-H_0-H_1-H_2)P_{01}$ matrix elements

The last exchange matrix element for each configuration interaction pair is

$$\langle j_0'k_0'(0),\phi_\alpha(1)\phi_\beta(2)(J_T') : J'M_{J'}|(E-H_0-H_1-H_2) \times P_{01}|j_0k_0(0),\phi_\gamma(1)\phi_\delta(2)(J_T) : JM_J\rangle. \tag{A19}$$

We apply P_{01} to the right-hand side to obtain

$$\begin{aligned}&\langle j_0'k_0'(0),\phi_\alpha(1)\phi_\beta(2)(J_T') : J'M_{J'}|(E-H_0-H_1-H_2)|j_0k_0(1),\phi_\gamma(0)\phi_\delta(2)(J_T) : JM_J\rangle \\ &= \frac{1}{\pi}\sqrt{\frac{(\epsilon_{k'}+c^2)(\epsilon_k+c^2)}{\epsilon_{k'}\epsilon_k}}\left\{\hat{J}_T'\hat{J}_T(-1)^{j_0+J_T+j_\gamma+J_T'}\begin{Bmatrix} j_0 & j_\delta & J_T' \\ j_\gamma & J & J_T\end{Bmatrix}\right. \\ &\times\left[\langle\phi_\alpha|j_0k\rangle\langle\phi_\beta|\phi_\delta\rangle\langle j_0'k'|\phi_\gamma\rangle[E(1-\theta)-\epsilon_{k'}-\epsilon_k]-\langle\phi_\alpha|j_0k\rangle\langle\phi_\beta|\phi_\delta\rangle\langle j_0'k'|(V_0-U_0)|\phi_\gamma\rangle\right. \\ &\left.\left.-\langle j_0'k'|\phi_\gamma\rangle\langle\phi_\beta|\phi_\delta\rangle\langle\phi_\alpha|(V_1-U_1)|j_0k\rangle-\langle j_0'k'|\phi_\gamma\rangle\langle\phi_\alpha|j_0k\rangle\langle\phi_\beta|(H_2)|\phi_\delta\rangle\right]-E\theta\langle j_0'k'|I_0^N|j_0k\rangle\langle\phi_\beta|\phi_\delta\rangle\langle\phi_\alpha|\phi_\gamma\rangle\right\}.\end{aligned} \tag{A20}$$

The parameter θ has been introduced in a manner similar to the nonrelativistic case to ensure the numerical stability and uniqueness of the T matrix, as outlined in [39]. The projection operator $I_n^N = \sum_n |\phi_n\rangle\langle\phi_n|$ is made from the configuration interaction single particle states.

[1] D. V. Fursa and I. Bray, Phys. Rev. Lett. **100**, 113201 (2008).
[2] D. V. Fursa, C. J. Bostock, and I. Bray, Phys. Rev. A **80**, 022717 (2009).
[3] C. J. Bostock, D. V. Fursa, and I. Bray, Phys. Rev. A **80**, 052708 (2009).
[4] J. Kessler, *Polarized Electrons* (Springer, Berlin, 1985).
[5] J. Waymouth, *Electric Discharge Lamps* (MIT Press, Cambridge, MA, 1971).
[6] G. Lister, in *Low Temperature Plasma Physics: Fundamental Aspects and Applications*, edited by R. Hippler, S. Pfau, M. Schmidt, and K. H. Schoenbach (Wiley, New York, 2001), pp. 387–406.
[7] G. G. Lister, J. E. Lawler, W. P. Lapatovich, and V. A. Godyak, Rev. Mod. Phys. **76**, 541 (2004).
[8] S. D. Rockwood, Phys. Rev. A **8**, 2348 (1973).
[9] R. Panajotović, V. Pejčev, M. Konstantinović, D. Filipović, V. Bočvarski, and B. Marinković, J. Phys. B **26**, 1005 (1993).
[10] M. Zubek, N. Gulley, A. Danjo, and G. C. King, J. Phys. B **29**, 5927 (1996).
[11] D. V. Fursa, I. Bray, and G. Lister, J. Phys. B **36**, 4255 (2003).
[12] G. F. Hanne, V. Nickich, and M. Sohn, J. Phys. B **18**, 2037 (1985).
[13] T. W. Ottley and H. Kleinpoppen, J. Phys. B **8**, 621 (1975).
[14] N. M. Erdevdi, O. B. Shpenik, and V. S. Vukstich, Opt. Spectrosc. **95**, 529 (2003).

[15] D. S. Newman, M. Zubek, and G. C. King, J. Phys. B **18**, 985 (1985).
[16] W. L. Borst, Phys. Rev. **181**, 257 (1969).
[17] H. F. Krause, S. G. Johnson, and S. Datz, Phys. Rev. A **15**, 611 (1977).
[18] F. J. Peitzmann and J. Kessler, J. Phys. B **23**, 2629 (1990).
[19] G. Holtkamp, K. Jost, F. J. Peitzmann, and J. Kessler, J. Phys. B **20**, 4543 (1987).
[20] K. Jost and B. Ohnemus, Phys. Rev. A **19**, 641 (1979).
[21] M. Zubek, A. Danjo, and G. C. King, J. Phys. B **28**, 4117 (1995).
[22] M. T. Elford, Aust. J. Phys. **33**, 251 (1980).
[23] J. P. England and M. T. Elford, Aust. J. Phys. **44**, 647 (1991).
[24] D. W. Walker, Adv. Phys. **20**, 257 (1971).
[25] R. P. McEachran and A. D. Stauffer, J. Phys. B **20**, 5517 (1987).
[26] J. E. Sienkiewicz, J. Phys. B **23**, 1869 (1990).
[27] J. E. Sienkiewicz, J. Phys. B **30**, 1261 (1997).
[28] R. P. McEachran and M. T. Elford, J. Phys. B **36**, 427 (2003).
[29] R. Haberland and L. Fritsche, J. Phys. B **20**, 121 (1987).
[30] N. S. Scott, P. G. Burke, and K. Bartschat, J. Phys. B **16**, L361 (1983).
[31] K. Bartschat, N. S. Scott, K. Blum, and P. G. Burke, J. Phys. B **17**, 269 (1984).
[32] K. Bartschat, in *Proceedings of the 3rd International Conference on Atomic and Molecular Data*, edited by F. O. D. R. Schultz and P. S. Krstic (American Institute of Physics, New York, 2002).
[33] W. P. Wijesundera, I. P. Grant, and P. H. Norrington, J. Phys. B **25**, 2143 (1992).
[34] K. Bartschat and D. H. Madison, J. Phys. B **20**, 1609 (1987).
[35] R. Srivastava, T. Zuo, R. P. McEachran, and A. D. Stauffer, J. Phys. B **26**, 1025 (1993).
[36] O. Zatsarinny and K. Bartschat, Phys. Rev. A **79**, 042713 (2009).
[37] K. G. Dyall, I. P. Grant, C. T. Johnson, F. P. Parpia, and E. P. Plummer, Comput. Phys. Commun. **55**, 425 (1989).
[38] I. P. Grant and H. M. Quiney, Phys. Rev. A **62**, 022508 (2000).
[39] D. V. Fursa and I. Bray, Phys. Rev. A **52**, 1279 (1995).
[40] [http://www.nist.gov/].
[41] T. M. Miller and B. Bederson, Adv. At. Mol. Phys. **13**, 1 (1977).
[42] L. S. Blackford *et al.*, *ScaLAPACK user's guide* (Society for Industrial and Applied Mathematics, Philadelphia, 1997).
[43] G. F. Hanne, Am. J. Phys. **56**, 696 (1988).
[44] J. P. Sullivan, P. D. Burrow, D. S. Newman, K. Bartschat, J. A. Michejda, R. Panajotovic, M. Moghbelalhossein, R. P. McEachran, and S. J. Buckman, New J. Phys. **5**, 159 (2003).
[45] I. Bray, D. V. Fursa, and I. E. McCarthy, J. Phys. B **27**, L421 (1994).
[46] A. R. Edmonds, *Angular Momentum in Quantum Mechanics* (Princeton University Press, Princeton, NJ, 1957).